Research Article Vol. 28, No. 3 / 3 February 2020 / Optics Express 2661
Optics EXPRESS

Deriving consistent ocean biological and biogeochemical products from multiple satellite ocean color sensors

MENGHUA WANG,[1,*] LIDE JIANG,[1,2] SEUNGHYUN SON,[1,2] XIAOMING LIU,[1,2] AND KENNETH J. VOSS[3]

[1]NOAA/NESDIS Center for Satellite Applications and Research, 5830 University Research Ct., College Park, Maryland 20740, USA
[2]CIRA at Colorado State University, Fort Collins, Colorado 80521, USA
[3]Physics Department, University of Miami, Coral Gables, Florida 33146, USA
[*]Menghua.Wang@noaa.gov

Abstract: A methodology is developed for deriving consistent ocean biological and biogeochemical products from multiple satellite ocean color sensors that have slightly different sensor spectral characteristics. Specifically, the required coefficients for algorithm modifications are obtained using the hyperspectral in situ optical measurements from the Marine Optical Buoy (MOBY) in the water off Hawaii. It is demonstrated that using the proposed approach for modifying ocean biological and biogeochemical algorithms, satellite-derived ocean property data over the global open ocean are consistent from multiple satellite sensors, although their corresponding sensor-measured normalized water-leaving radiance spectra $nL_w(\lambda)$ are different. Therefore, the proposed approach allows satellite-derived ocean biological and biogeochemical products to be consistent and can therefore be routinely merged from various satellite ocean color sensors. The proposed approach can be applied to any satellite algorithms that use the input of sensor-measured $nL_w(\lambda)$ spectra.

1. Introduction

For ocean color remote sensing, after carrying out atmospheric correction [1–5], satellite sensors measure normalized water-leaving radiance $nL_w(\lambda)$ spectra or normalized water-leaving reflectance $\rho_{wN}(\lambda)$ [or remote sensing reflectance $R_{rs}(\lambda)$] spectra, which are defined as $\rho_{wN}(\lambda) = \pi nL_w(\lambda)/F_0(\lambda)$ and $R_{rs}(\lambda) = \rho_{wN}(\lambda)/\pi$, with $F_0(\lambda)$ the extraterrestrial solar irradiance [6]. The sensor spectral bands chosen are those sensitive to water biological and biogeochemical properties, which allow these properties to be derived from satellite-measured $nL_w(\lambda)$ spectra. Effectively, satellite-derived $nL_w(\lambda)$ spectra are the same as (or close to) those measured directly on the ocean surface assuming that there was no atmosphere and the Sun at the nadir [1,3,7–9]. However, even for the same series of satellite sensors, e.g., the Visible Infrared Imaging Radiometer Suite (VIIRS) [10] on the Suomi National Polar-orbiting Partnership (SNPP) (2011–present), NOAA-20 (N20) (2017–present), and the Joint Polar Satellite System (JPSS) three follow-on VIIRS sensors in the future, the sensor spectral characteristics will always have some differences. For satellite sensors from different space agencies (or from a different series of instruments), the spectral band differences may be large even though they are all designed for ocean color remote sensing, e.g., comparing ocean color sensors among VIIRS [10], the Sea-viewing Wild Field-of-view Sensor (SeaWiFS) [11], the Moderate Resolution Imaging Spectroradiometer (MODIS) [12,13] on the Terra and Aqua, the Medium-Resolution Imaging Spectrometer (MERIS) [14] on the Envisat, the Ocean and Land Colour Instrument (OLCI) [15] on the Sentinel-3A (S3A) and Sentinel-3B (S3B), the Second-Generation Global Imager (SGLI) on the Global Change Observation Mission-Climate (GCOM-C) satellite, and others (e.g., the Geostationary

#376238 https://doi.org/10.1364/OE.376238
Journal © 2020 Received 26 Aug 2019; revised 20 Dec 2019; accepted 8 Jan 2020; published 21 Jan 2020

Optics EXPRESS

Ocean Color Imager (GOCI) [16,17]). In particular, sensor spectral response function (SRF) (i.e., sensor spectral response or measurement as a function of wavelength) differences from the two different VIIRS sensors (or from VIIRS and OLCI or SGLI) can have different sensor-measured $nL_w(\lambda)$ spectra [18], which if ignored will lead to differences in satellite-derived biological and biogeochemical products, e.g., chlorophyll-a (Chl-a) concentration [19–21], water diffuse attenuation coefficient at the wavelength of 490 nm $K_d(490)$ [22–24] or at the photosynthetically available radiation (PAR) $K_d(\text{PAR})$ [24,25], etc. These differences are often noticeable and sometimes significant, making it difficult to produce consistent data products and merge data directly from multiple satellite sensors.

Satellite algorithms for deriving ocean biological and biogeochemical products, which are computed from the input of sensor-measured $nL_w(\lambda)$ [or $\rho_{\text{wN}}(\lambda)$] spectra, can be adjusted and modified based on the sensor spectral characteristics (i.e., SRFs). For example, Chl-a algorithms for SeaWiFS, MODIS, MERIS, and other sensors have been developed [26,27] and used for deriving global open ocean Chl-a products. Specifically, coefficients for Chl-a algorithms for different satellite sensors (different sensor SRFs) are adjusted and modified for the specific set of spectral bands corresponding to a specific satellite sensor. Therefore, consistent Chl-a data can be derived using the same Chl-a algorithm (but with different empirical fitting coefficients) for different satellite sensors, e.g., the Chl-a algorithm OC4 for SeaWiFS, OC3M for MODIS, OC4E for MERIS, etc. [26,27]. In principle, such a coefficient adjustment approach to account for differences in sensor SRFs could always be carried out if there were enough good quality in situ biological and biogeochemical data with the corresponding in situ hyperspectral $nL_w(\lambda)$ data (for accounting for the differences in sensor SRFs). However, the approach is not always straightforward for satellite optical, biological, and biogeochemical algorithms with limited high quality in situ data and limited spectral coverage over the global ocean, e.g., $K_d(490)$ data, inherent optical property (IOP) data [28–31], suspended particulate matter (SPM) data [32], or other new ocean property products that lack the in situ data with the corresponding hyperspectral $nL_w(\lambda)$ [or $\rho_{\text{wN}}(\lambda)$] spectra.

In this paper, a methodology to account for sensor SRF differences in satellite biological and biogeochemical algorithms (or any other algorithms using the input of $nL_w(\lambda)$ spectra) is proposed and described. Specifically, the effect of satellite-derived $nL_w(\lambda)$ [or $\rho_{\text{wN}}(\lambda)$] spectra from different satellite sensors (with different SRFs) are first accurately accounted for using the in situ optics measurements from the Marine Optical Buoy (MOBY) in the water off Hawaii [33] (https://coastwatch.noaa.gov/cw/field-observations/MOBY.html). It should be noted that, because of the sensor SRF effect, satellites actually measure the sensor SRF-weighted $nL_w(\lambda)$ spectra [18]. MOBY in situ hyperspectral $nL_w(\lambda)$ measurements over the entire visible spectral wavelengths make it possible to compute sensor SRF-weighted $nL_w(\lambda)$ spectra for any given satellite ocean color sensor. Thus, the spectral effect on satellite-derived $nL_w(\lambda)$ spectra for various satellite ocean color sensors can be accurately calculated. In fact, the formulations to account for differences in the specific sensor spectral characteristics for satellite biological and biogeochemical algorithms (or any other $nL_w(\lambda)$-based algorithms) are rigorous, with appropriate coefficients derived from the MOBY in situ data. Therefore, the approach can be used for any satellite sensors and for any optical, biological, and biogeochemical algorithms that use the input of satellite-derived $nL_w(\lambda)$ spectra. Results of Chl-a and $K_d(490)$ from VIIRS-SNPP and VIIRS-N20 are provided and discussed, showing that consistent ocean color data from the two sensors can be obtained using the proposed approach. In addition, some results (particularly required coefficients) and discussions for deriving consistent Chl-a and $K_d(490)$ from satellite ocean color sensors of VIIRS, OLCI, and SGLI are provided.

Optics EXPRESS

2. Methodology

In this section, the approach to deal with the sensor spectral band differences in Chl-a and $K_d(490)$ algorithms from different satellite ocean color sensors is outlined. Specifically, the required modifications for Chl-a and $K_d(490)$ algorithms for VIIRS-N20, OLCI-S3A, and SGLI-GCOM-C to derive Chl-a and $K_d(490)$ products consistently with those from VIIRS-SNPP are described and discussed. It is noted that in this study all satellite data processing are carried out using the Multi-Sensor Level-1 to Level-2 (MSL12) ocean color data processing system [34], which is the NOAA official VIIRS ocean color data processing system. MSL12 is an enterprise satellite ocean color data processing system, capable of processing ocean color product data consistently from multiple satellite ocean color sensors [35–37].

2.1. Chl-a algorithms

2.1.1. The OC3 V algorithm

Over the global open ocean, the distribution of phytoplankton Chl-a has been measured from space using the empirical regressions of spectral reflectance ratios in normalized water-leaving reflectance $\rho_{wN}(\lambda)$ [or remote sensing reflectance $R_{rs}(\lambda)$] at the blue and green bands [19,27,38,39]. In particular, the traditional VIIRS-SNPP Chl-a algorithm is based on the ocean chlorophyll-type (OCx) [19] using $\rho_{wN}(\lambda)$ at the wavelengths of 443, 486, and 551 nm, corresponding to the VIIRS M2, M3, and M4 bands. The VIIRS three-band blue-green reflectance ratio algorithm is named as OC3V [34]. Similar empirical Chl-a algorithms exist for SeaWiFS (e.g., the OC2 and OC4 Chl-a algorithms) and MODIS (e.g., the OC3M Chl-a algorithm) [26]. Specifically, the OC3V algorithm for VIIRS can be written as:

$$Chl\text{-}a = 10^{\sum_{i=0}^{i=4} a_i X^i}, \tag{1}$$

with

$$X = max\left[\log_{10}\left(\frac{\rho_{wN}(\mathrm{M2})}{\rho_{wN}(\mathrm{M4})}\right), \log_{10}\left(\frac{\rho_{wN}(\mathrm{M3})}{\rho_{wN}(\mathrm{M4})}\right)\right], \tag{2}$$

where ρ_{wN}(M2), ρ_{wN}(M3), and ρ_{wN}(M4) are corresponding to VIIRS-derived $\rho_{wN}(\lambda)$ at spectral bands of M2, M3, and M4, respectively. The above Eq. (2) takes a larger value of two reflectance ratios in logarithmic scale. The five coefficients a_0 to a_4 are the best fitting coefficients for the three-band empirical Chl-a algorithm from in situ measurements [19,26]. Specifically, for VIIRS-SNPP these five coefficients are 0.2228, −2.4683, 1.5867, −0.4275, and −0.7768. For convenience in discussion, Chl-a concentration data (or any parameter Y) derived from VIIRS-SNPP (SNPP) and VIIRS-NOAA-20 (N20) are noted as $[\text{Chl-a}]^{(\mathrm{SNPP})}$ and $[\text{Chl-a}]^{(\mathrm{N20})}$ (or $[Y]^{(\mathrm{SNPP})}$ and $[Y]^{(\mathrm{N20})}$), respectively. It is noted that the discussion can be applied to any two sensors, i.e., one can simply treat "SNPP" and "N20" as names from any two sensors, e.g., sensors A and B.

Using Eqs. (1) and (2), Chl-a data from VIIRS-SNPP and VIIRS-N20 can be derived. However, due to slight differences in sensor SRFs, $X^{(\mathrm{SNPP})}$ and $X^{(\mathrm{N20})}$ values in Eq. (2) are generally different for the two VIIRS sensors, leading to different Chl-a values from the two satellite sensors. It should be emphasized that differences in satellite-derived Chl-a data using Eqs. (1) and (2) are due to sensor SRF differences from the two sensors, not from real measurements. This difference in satellite-derived Chl-a is certainly not reasonable and desirable, and therefore requires algorithm corrections and modifications.

To derive consistent Chl-a data from the two VIIRS sensors that have slightly different sensor SRFs, Eq. (2) for VIIRS-N20 can be specifically written as the same formula as for VIIRS-SNPP

Optics EXPRESS

but with $\rho_{wN}(\lambda)$ inputs from VIIRS-N20, i.e.,

$$X^{(\mathrm{N20})} = max\left[\log_{10}\left(r_{24}\left[\left(\frac{\rho_{wN}(\mathrm{M2})}{\rho_{wN}(\mathrm{M4})}\right)\right]^{(\mathrm{N20})}\right), \log_{10}\left(r_{34}\left[\left(\frac{\rho_{wN}(\mathrm{M3})}{\rho_{wN}(\mathrm{M4})}\right)\right]^{(\mathrm{N20})}\right)\right], \tag{3}$$

with coefficients r_{24} and r_{34} are:

$$r_{24} = \left[\left(\frac{\rho_{wN}(\mathrm{M2})}{\rho_{wN}(\mathrm{M4})}\right)\right]^{(\mathrm{SNPP})} / \left[\left(\frac{\rho_{wN}(\mathrm{M2})}{\rho_{wN}(\mathrm{M4})}\right)\right]^{(\mathrm{N20})} \text{ and } r_{34} = \left[\left(\frac{\rho_{wN}(\mathrm{M3})}{\rho_{wN}(\mathrm{M4})}\right)\right]^{(\mathrm{SNPP})} / \left[\left(\frac{\rho_{wN}(\mathrm{M3})}{\rho_{wN}(\mathrm{M4})}\right)\right]^{(\mathrm{N20})}. \tag{4}$$

Therefore, using Eqs. (1), (3), and (4) with the inputs from VIIRS-N20-measured $\rho_{wN}(\lambda)$ values, Chl-a data derived from VIIRS N20 and SNPP are now consistent, i.e., we have forced (or adjusted) $X^{(\mathrm{N20})} = X^{(\mathrm{SNPP})}$, eliminating the effects of the SRF differences from the two sensors. Using Eqs. (3) and (4) for VIIRS-N20 Chl-a computation, there are no biases in satellite-derived Chl-a data due to slight differences in sensor spectral band characteristics from the two sensors. In fact, with the modifications in Eqs. (3) and (4), Chl-a algorithms for VIIRS-SNPP and VIIRS-N20 are exactly the same, assuming that coefficients r_{24} and r_{34} in Eq. (4) can be derived accurately. It is particularly noted that these equations are derived rigorously.

2.1.2. The OCI algorithm

To improve the Chl-a data quality over global oligotrophic waters, the ocean color index (OCI) algorithm has been developed [20]. The OCI Chl-a algorithm has also been implemented in MSL12 for VIIRS global ocean color data processing with an improved Chl-a data merging method between the color index (CI)-based and OC3V-based Chl-a algorithms [21]. Indeed, the VIIRS OCI Chl-a algorithm combines the CI and OC3V Chl-a algorithms for the global open ocean and shows improvements over global clear (oligotrophic) ocean regions [19–21,26]. Specifically, the VIIRS-SNPP CI-based Chl-a algorithm can be written as [21]:

$$\begin{aligned} &[Chl\text{-}a]_{\mathrm{CI}}^{(\mathrm{SNPP})} = 10^{216.76\times CI^{(\mathrm{SNPP})}-0.4093} \text{ and} \\ &CI^{(\mathrm{SNPP})} = [R_{rs}(\mathrm{M4})]^{(\mathrm{SNPP})} - 0.526\,[R_{rs}(\mathrm{M2})]^{(\mathrm{SNPP})} - 0.474\,[R_{rs}(\mathrm{M5})]^{(\mathrm{SNPP})} \end{aligned}, \tag{5}$$

with the parameter $CI^{(\mathrm{SNPP})}$ computed from VIIRS-SNPP-measured remote-sensing reflectance $[R_{rs}(\lambda)]^{(\mathrm{SNPP})}$ at the bands M2 (443 nm), M4 (551 nm), and M5 (671 nm) [21]. Therefore, the VIIRS-SNPP OCI Chl-a algorithm can be written as [21],

$$\begin{aligned} &[Chl\text{-}a]_{\mathrm{OCI}}^{(\mathrm{SNPP})} = [Chl\text{-}a]_{\mathrm{CI}}^{(\mathrm{SNPP})} \text{ for } [r]^{(\mathrm{SNPP})}>4, \\ &[Chl\text{-}a]_{\mathrm{OCI}}^{(\mathrm{SNPP})} = w\,[Chl\text{-}a]_{\mathrm{CI}}^{(\mathrm{SNPP})} + (1-w)\,[Chl\text{-}a]_{\mathrm{OC3V}}^{(\mathrm{SNPP})} \text{ for } 2<[r]^{(\mathrm{SNPP})} \le 4, \text{ and} \\ &[Chl\text{-}a]_{\mathrm{OCI}}^{(\mathrm{SNPP})} = [Chl\text{-}a]_{\mathrm{OC3V}}^{(\mathrm{SNPP})} \text{ for } [r]^{(\mathrm{SNPP})} \le 2, \end{aligned} \tag{6}$$

where $[Chl\text{-}a]_{\mathrm{OC3V}}^{(\mathrm{SNPP})}$ and $[Chl\text{-}a]_{\mathrm{CI}}^{(\mathrm{SNPP})}$ are Chl-a concentration derived from the OC3V [Eqs. (1) and (2)] and the CI [Eq. (5)] Chl-a algorithm, respectively. In Eq. (6), the remote-sensing reflectance ratio $[r]^{(\mathrm{SNPP})}$ from the VIIRS-SNPP bands M2 and M4 is used for the weight w computation [21], i.e.,

$$\begin{aligned} &w = 0.5\,([r]^{(\mathrm{SNPP})} - 2) \text{ for } 2<[r]^{(\mathrm{SNPP})} \le 4, \\ &w = 0 \text{ for } [r]^{(\mathrm{SNPP})} \le 2, \text{ and} \\ &w = 1 \text{ for } [r]^{(\mathrm{SNPP})}>4 \text{ with } [r]^{(\mathrm{SNPP})} = \frac{[R_{rs}(\mathrm{M2})]^{(\mathrm{SNPP})}}{[R_{rs}(\mathrm{M4})]^{(\mathrm{SNPP})}}. \end{aligned} \tag{7}$$

Using the same approach as discussed in the previous section for the OC3V Chl-a algorithm with inputs from the VIIRS-N20-measured $[R_{rs}(\lambda)]^{(\mathrm{N20})}$ at the bands M2 (443 nm), M4 (556 nm), and

Optics EXPRESS

M5 (667 nm), the CI-based Chl-a algorithm for VIIRS-N20 can be written as:

$$[Chl\text{-}a]_{\mathrm{CI}}^{(\mathrm{N20})} = 10^{216.76\times CI^{(\mathrm{N20})}-0.4093}, \text{ and}$$

$$CI^{(\mathrm{N20})} = r_4 \cdot [R_{rs}(\mathrm{M4})]^{(\mathrm{N20})} - r_2 \cdot 0.526\ [R_{rs}(\mathrm{M2})]^{(\mathrm{N20})} - \ r_5 \cdot 0.474\ [R_{rs}(\mathrm{M5})]^{(\mathrm{N20})}, \tag{8}$$

where

$$r_2 = \frac{[R_{rs}(\mathrm{M2})]^{(\mathrm{SNPP})}}{[R_{rs}(\mathrm{M2})]^{(\mathrm{N20})}},\ r_4 = \frac{[R_{rs}(\mathrm{M4})]^{(\mathrm{SNPP})}}{[R_{rs}(\mathrm{M4})]^{(\mathrm{N20})}},\ \text{and}\ r_5 = \frac{[R_{rs}(\mathrm{M5})]^{(\mathrm{SNPP})}}{[R_{rs}(\mathrm{M5})]^{(\mathrm{N20})}}. \tag{9}$$

Therefore, it is now straightforward to also write the merged OCI Chl-a algorithm for VIIRS-N20, i.e.,

$$\begin{aligned}
&[Chl\text{-}a]_{\mathrm{OCI}}^{(\mathrm{N20})} = [Chl\text{-}a]_{\mathrm{CI}}^{(\mathrm{N20})} \ \text{for}\ r_{24}\cdot[r]^{(\mathrm{N20})}>4,\\
&[Chl\text{-}a]_{\mathrm{OCI}}^{(\mathrm{N20})} = w\,[Chl\text{-}a]_{\mathrm{CI}}^{(\mathrm{N20})} + (1-w)\,[Chl\text{-}a]_{\mathrm{OC3V}}^{(\mathrm{N20})} \ \text{for}\ \ 2<r_{24}\cdot[r]^{(\mathrm{N20})}\le 4, \text{ and}\\
&[Chl\text{-}a]_{\mathrm{OCI}}^{(\mathrm{N20})} = [Chl\text{-}a]_{\mathrm{OC3V}}^{(\mathrm{N20})} \ \text{for}\ r_{24}\cdot[r]^{(\mathrm{N20})}\le 2,
\end{aligned} \tag{10}$$

where

$$[r]^{(\mathrm{N20})} = \frac{[R_{rs}(\mathrm{M2})]^{(\mathrm{N20})}}{[R_{rs}(\mathrm{M4})]^{(\mathrm{N20})}}, r_{24} = \frac{[R_{rs}(\mathrm{M2})]^{(\mathrm{SNPP})}}{[R_{rs}(\mathrm{M4})]^{(\mathrm{SNPP})}} \Big/ \frac{[R_{rs}(\mathrm{M2})]^{(\mathrm{N20})}}{[R_{rs}(\mathrm{M4})]^{(\mathrm{N20})}}, \tag{11}$$

and $[Chl\text{-}a]_{\mathrm{OC3V}}^{(\mathrm{N20})}$ and $[Chl\text{-}a]_{\mathrm{CI}}^{(\mathrm{N20})}$ are Chl-a data derived from VIIRS-N20 using the OC3 V [Eqs. (1) and (3)] and CI-based algorithm [Eqs. (8) and (9)], respectively, with effectively $r_{24}\cdot[r]^{(\mathrm{N20})} = [r]^{(\mathrm{SNPP})}$.

2.2. $K_d(490)$ algorithms

2.2.1. The $K_d(490)$ algorithm for the open ocean

Over global open oceans, the water diffuse attenuation coefficient at the wavelength of 490 nm, $K_d(490)$, can be derived using the satellite-measured $nL_w(\lambda)$ ratio at the two wavelengths between around 490 and 555 nm [24,40]. Specifically, for the open ocean, the $K_d(490)$ algorithm for VIIRS-SNPP can be written as:

$$[K_d(490)]^{(\mathrm{SNPP})} = A\left(\frac{[nL_w(\mathrm{M3})]^{(\mathrm{SNPP})}}{[nL_w(\mathrm{M4})]^{(\mathrm{SNPP})}}\right)^B, \tag{12}$$

with coefficients A and B of 0.1853 and −1.349, respectively. Therefore, using the same approach discussed previously for Chl-a algorithms in Section 2.1, the open ocean $K_d(490)$ algorithm for VIIRS-N20 can be written as:

$$[K_d(490)]^{(\mathrm{N20})} = A\left(c_{34}\times\frac{[nL_w(\mathrm{M3})]^{(\mathrm{N20})}}{[nL_w(\mathrm{M4})]^{(\mathrm{N20})}}\right)^B, \text{ with} \tag{13}$$

$$c_{34} = \frac{[nL_w(\mathrm{M3})]^{(\mathrm{SNPP})}}{[nL_w(\mathrm{M4})]^{(\mathrm{SNPP})}} \Big/ \frac{[nL_w(\mathrm{M3})]^{(\mathrm{N20})}}{[nL_w(\mathrm{M4})]^{(\mathrm{N20})}}. \tag{14}$$

Therefore, using Eqs. (13) and (14) for deriving $K_d(490)$ over the global open ocean for VIIRS-N20, VIIRS-N20-derived $K_d(490)$ data are consistent with those from VIIRS-SNPP. The effect of slight differences in SRFs from the two VIIRS sensors is now accurately accounted for. Indeed, the open ocean $K_d(490)$ algorithm for VIIRS-N20 is effectively calculated to be the same as that for VIIRS-SNPP, i.e., $[K_d(490)]^{(\mathrm{N20})} = [K_d(490)]^{(\mathrm{SNPP})}$.

Optics EXPRESS

2.2.2. The $K_d(490)$ algorithm for coastal and inland waters

For turbid coastal and inland waters, the *Wang et al.* (2009) [22] $K_d(490)$ algorithm has been implemented in MSL12 and used for routine production of VIIRS global $K_d(490)$ data. Specifically, VIIRS-measured spectral irradiance reflectance just beneath the sea surface $R(\lambda)$ at the bands M3 and M5 [R(M3) and R(M5)] are used, with $R(\lambda)$ given by [28,39,41]

$$R(\lambda) = \frac{4\ nL_w(\lambda)}{0.52\ F_0(\lambda) + 1.7\ nL_w(\lambda)}, \tag{15}$$

where $F_0(\lambda)$ is the extraterrestrial solar irradiance [6] at a given wavelength λ. Using $R(\lambda)$ at the VIIRS bands M3 and M5, the same formulation (the Eq. (9) of *Wang et al.* (2009) [22]) $K_d(490)$ algorithm can be directly used for both VIIRS-SNPP and VIIRS-N20. Therefore, we only need to compute proper $R(\lambda)$ values for VIIRS-N20 (i.e., to be consistent with those from VIIRS-SNPP). Specifically, for VIIRS-SNPP reflectance $R(\lambda)$ is given by [42]

$$[R(\lambda)]^{(\mathrm{SNPP})} = \frac{4\ [nL_w(\lambda)]^{(\mathrm{SNPP})}}{0.52\ [F_0(\lambda)]^{(\mathrm{SNPP})} + 1.7\ [nL_w(\lambda)]^{(\mathrm{SNPP})}} \tag{16}$$

and the above Eq. (16) can be re-written for VIIRS-N20 as

$$[R(\lambda)]^{(\mathrm{N20})} = \frac{4\ [nL_w(\lambda)]^{(\mathrm{N20})}}{0.52\ [F_0(\lambda)]^{(\mathrm{N20})} \times ([\rho_{wN}(\lambda)]^{(\mathrm{N20})}/[\rho_{wN}(\lambda)]^{(\mathrm{SNPP})}) + 1.7\ [nL_w(\lambda)]^{(\mathrm{N20})}}, \tag{17}$$

with now effectively $[R(\lambda)]^{(\mathrm{N20})} = [R(\lambda)]^{(\mathrm{SNPP})}$. Therefore, particularly for VIIRS-N20 irradiance reflectance just beneath the surface $R(\lambda)$ at the bands M3 and M5, Eq. (17) becomes

$$[R(\mathrm{M3})]^{(\mathrm{N20})} = \frac{4\ [nL_w(\mathrm{M3})]^{(\mathrm{N20})}}{0.52\ [F_0(\mathrm{M3})]^{(\mathrm{N20})} \times b_3 + 1.7\ [nL_w(\mathrm{M3})]^{(\mathrm{N20})}} \text{ and} \tag{18}$$

$$[R(\mathrm{M5})]^{(\mathrm{N20})} = \frac{4\ [nL_w(\mathrm{M5})]^{(\mathrm{N20})}}{0.52\ [F_0(\mathrm{M5})]^{(\mathrm{N20})} \times b_5 + 1.7\ [nL_w(\mathrm{M5})]^{(\mathrm{N20})}}, \tag{19}$$

with coefficients b_3 and b_5 given by

$$b_3 = \frac{[\rho_{wN}(\mathrm{M3})]^{(\mathrm{N20})}}{[\rho_{wN}(\mathrm{M3})]^{(\mathrm{SNPP})}} \text{ and } \quad b_5 = \frac{[\rho_{wN}(\mathrm{M5})]^{(\mathrm{N20})}}{[\rho_{wN}(\mathrm{M5})]^{(\mathrm{SNPP})}}. \tag{20}$$

In addition, there is a weight W computation (the Eq. (14) of *Wang et al.* (2009) [22]) for the merged $K_d(490)$ algorithm applying for both open ocean and turbid coastal/inland waters [22], i.e., for VIIRS-SNPP the weight is calculated as

$$[W]^{(\mathrm{SNPP})} = -1.175 + 4.512 \cdot \frac{[R_{rs}(\mathrm{M5})]^{(\mathrm{SNPP})}}{[R_{rs}(\mathrm{M3})]^{(\mathrm{SNPP})}} \text{ for } 0.2604 \ \le \ \frac{[R_{rs}(\mathrm{M5})]^{(\mathrm{SNPP})}}{[R_{rs}(\mathrm{M3})]^{(\mathrm{SNPP})}} \ \le 0.4821. \tag{21}$$

Similarly, converting the above Eq. (21) to VIIRS-N20, the weight formulation (the Eq. (14) of *Wang et al.* (2009) [22]) for VIIRS-N20 is modified to

$$[W]^{(\mathrm{N20})} = -1.175 + r_{53} \cdot 4.512 \frac{[R_{rs}(\mathrm{M5})]^{(\mathrm{N20})}}{[R_{rs}(\mathrm{M3})]^{(\mathrm{N20})}} \text{ for } 0.2604 \ \le \ r_{53} \frac{[R_{rs}(\mathrm{M5})]^{(\mathrm{N20})}}{[R_{rs}(\mathrm{M3})]^{(\mathrm{N20})}} \ \le 0.4821, \tag{22}$$

where

$$r_{53} = \left[\left(\frac{\rho_{wN}(\mathrm{M5})}{\rho_{wN}(\mathrm{M3})}\right)\right]^{(\mathrm{SNPP})} / \left[\left(\frac{\rho_{wN}(\mathrm{M5})}{\rho_{wN}(\mathrm{M3})}\right)\right]^{(\mathrm{N20})}. \tag{23}$$

Obviously, with the modifications of the weight computation in Eqs. (22) and (23), the weights derived from the two VIIRS sensors are effectively the same, i.e., $[W]^{(\mathrm{N20})} = [W]^{(\mathrm{SNPP})}$.

Optics EXPRESS

2.3. Coefficients derived from the MOBY in situ data

2.3.1. VIIRS-N20 and VIIRS-SNPP

Using the MOBY in situ hyperspectral optical measurements in the water off Hawaii [33], all required coefficients can be accurately derived for the open ocean. In fact, VIIRS SRF-weighted MOBY in situ $nL_w(\lambda)$ [or $\rho_{wN}(\lambda)$] data for both VIIRS-SNPP and VIIRS-N20 have been routinely produced since the two VIIRS launched in October 2011 and November 2017, respectively. Therefore, ratios of MOBY in situ-derived $nL_w(\lambda)$ [or $\rho_{wN}(\lambda)$] between the two VIIRS sensors can be computed. Figure 1 provides scatter plots of the MOBY-measured $nL_w(\lambda)$ between VIIRS-N20 and VIIRS-SNPP, showing very strong correlations in $nL_w(\lambda)$ from the two VIIRS sensors (as expected). Figure 1(a) shows results of MOBY-measured in situ $nL_w(\lambda)$ in VIIRS-N20 (SRF-weighted) compared with those from VIIRS-SNPP (SRF-weighted) for the VIIRS spectral bands at M1–M3, while Fig. 1(b) is comparison results for the VIIRS bands at M4, I1, and M5. In fact, results in Fig. 1 show that over the MOBY site (open ocean waters) in situ MOBY-measured $nL_w(\lambda)$ at the bands M1 and M2 are nearly identical between SNPP and NOAA-20, while they are differed by about 5%, 16%, 15%, and 21% for bands M3, M4, I1, and M5, respectively. It is important to note that as expected the two MOBY-measured $nL_w(\lambda)$ [or $\rho_{wN}(\lambda)$] spectra for VIIRS-SNPP and VIIRS-N20 are strongly correlated (Fig. 1), and thus can be related to each other. It is also noted that, although sensor SRF data are used for computations, all data in Fig. 1 are really from MOBY in situ measurements.

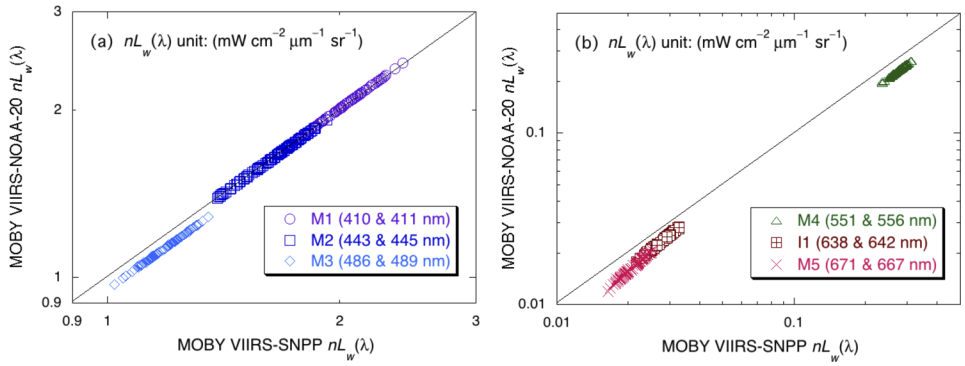

Fig. 1. Scatter plots of MOBY-measured and sensor SRF-weighted $nL_w(\lambda)$ between VIIRS-N20 and VIIRS-SNPP for the VIIRS SNPP and N20 spectral bands of (a) 410 & 411 nm, 443 & 445 nm, and 486 & 489 nm and (b) 551 & 556 nm, 638 & 642 nm, and 671 & 667 nm.

Table 1 shows summary statistics [mean, median, and standard deviation (STD)] of MOBY in situ data (sensor SRF-weighted) for per-band comparison between VIIRS-N20 and VIIRS-SNPP. The first column in Table 1 shows the nominal center wavelengths (nm) for VIIRS-N20 and VIIRS-SNPP bands. The next three columns in Table 1 are for statistics in $nL_w(\lambda)$ ratio (mean, median, and STD) between VIIRS-N20 and VIIRS-SNPP. The last three columns in Table 1 are for statistics in $\rho_{wN}(\lambda)$ ratios (mean, median, and STD) between VIIRS-N20 and VIIRS-SNPP. With the ratio values of $nL_w(\lambda)$ and $\rho_{wN}(\lambda)$ from Table 1, all required coefficients in various equations for VIIRS-N20 Chl-a and $K_d(490)$ algorithms can be computed.

Using the median ratio values in Table 1 and taking VIIRS-SNPP as a reference sensor, all required coefficients for modifying Chl-a and $K_d(490)$ algorithms for VIIRS-N20 can be calculated. The required coefficient values are summarized in Table 2 with the corresponding applicable equations indicated. Thus, with the corresponding equations for Chl-a and $K_d(490)$ algorithms for VIIRS-N20, VIIRS-N20-derived Chl-a and $K_d(490)$ data are now consistent with those from VIIRS-SNPP.

Optics EXPRESS

Table 1. Statistics in ratios (mean, median, and STD) of MOBY-measured $nL_w(\lambda)$ and $\rho_{wN}(\lambda)$ between VIIRS-N20 and VIIRS-SNPP. The data number used is 200.

VIIRS Band (N20, SNPP) (nm)	MOBY $nL_w(\lambda)$ Ratio (N20 versus SNPP)			MOBY $\rho_{wN}(\lambda)$ Ratio (N20 versus SNPP)		
	Mean	Median	STD	Mean	Median	STD
M1 (411, 410)	1.0046	1.0046	0.0003	0.9942	0.9942	0.0003
M2 (445, 443)	0.9994	0.9993	0.0011	0.9876	0.9875	0.0011
M3 (489, 486)	0.9518	0.9514	0.0019	0.9572	0.9568	0.0019
M4 (556, 551)	0.8422	0.8410	0.0049	0.8493	0.8481	0.0050
M5 (667, 671)	0.7859	0.7870	0.0202	0.7824	0.7836	0.0201
I1 (642, 638)	0.8448	0.8454	0.0101	0.8540	0.8546	0.0102

Table 2. Coefficients needed for modifying various equations for the VIIRS-N20 Chl-a and $K_d(490)$ algorithms, which are calculated from Table 1 with median values.

Equation Number	Corresponding Coefficients
Eqs. (3) and (4)	$r_{24} = 0.8588$, $r_{34} = 0.8864$
Eqs. (8) and (9)	$r_2 = 1.0127$, $r_4 = 1.1791$, $r_5 = 1.2762$
Eq. (11)	$r_{24} = 0.8588$
Eq. (14)	$c_{34} = 0.8840$
Eqs. (18) and (20)	$b_3 = 0.9568$
Eqs. (19) and (20)	$b_5 = 0.7836$
Eqs. (22) and (23)	$r_{53} = 1.2210$

2.3.2. OLCI-S3A and VIIRS-SNPP

Similarly, using the OLCI-S3A (SRF-weighted) and VIIRS-SNPP (SRF-weighted) MOBY in situ $nL_w(\lambda)$ [or $\rho_{wN}(\lambda)$] data, $nL_w(\lambda)$ [or $\rho_{wN}(\lambda)$] ratio values between the two sensors for the corresponding spectral bands can be derived. Specifically, OLCI-S3A SRF-weighted MOBY $nL_w(\lambda)$ [or $\rho_{wN}(\lambda)$] at the bands with nominal center wavelengths of 413, 443, 490, 560 nm are compared with those of VIIRS-SNPP (SRF-weighted) bands (M1–M4) at the wavelengths of 410, 443, 486, and 551 nm. However, OLCI-S3A has three spectral bands at around the red wavelength (i.e., 665, 674, and 681 nm) corresponding to the VIIRS-SNPP red band at 671 nm. These $nL_w(\lambda)$ [or $\rho_{wN}(\lambda)$] (with specific sensor SRF weighted) ratio values at the three OLCI red bands versus the VIIRS-SNPP red band at 671 nm can be derived using the MOBY hyperspectral in situ optical measurements.

Figure 2 shows the scatter plots of the MOBY-measured in situ $nL_w(\lambda)$ (with specific sensor SRF-weighted) between OLCI-S3A and VIIRS-SNPP. Figure 2(a) is for $nL_w(\lambda)$ at the OLCI spectral bands of 413, 443, and 490 nm corresponding to the VIIRS-SNPP $nL_w(\lambda)$ at the spectral bands of 410, 443, and 486 nm, respectively, while Fig. 2(b) is for the OLCI SRF-weighted MOBY $nL_w(\lambda)$ at the bands of 560, 665, 674, and 681 nm compared with those from VIIRS-SNPP SRF-weighted MOBY $nL_w(\lambda)$ at the spectral bands of 551, 671, 671, and 671 nm, respectively. As discussed, VIIRS only has one red band (671 nm for SNPP and 667 nm for N20), compared with the three bands from OLCI. Results in Fig. 2 show that for the short blue and blue bands OLCI-S3A and VIIRS-SNPP have almost identical spectral characteristics ($< \sim 1\%$), while some large differences are shown in other bands, in particular, for the green band ($\sim 23\%$). However, again as expected, OLCI-SRF-weighted and VIIRS-SRF-weighted MOBY $nL_w(\lambda)$ [or $\rho_{wN}(\lambda)$] spectra are generally strongly correlated (Fig. 2).

Same as in Table 1 for VIIRS-N20 and VIIRS-SNPP, Table 3 provides the statistics in ratio values of the MOBY-measured and sensor SRF-weighted in situ $nL_w(\lambda)$ and $\rho_{wN}(\lambda)$ between

Optics EXPRESS

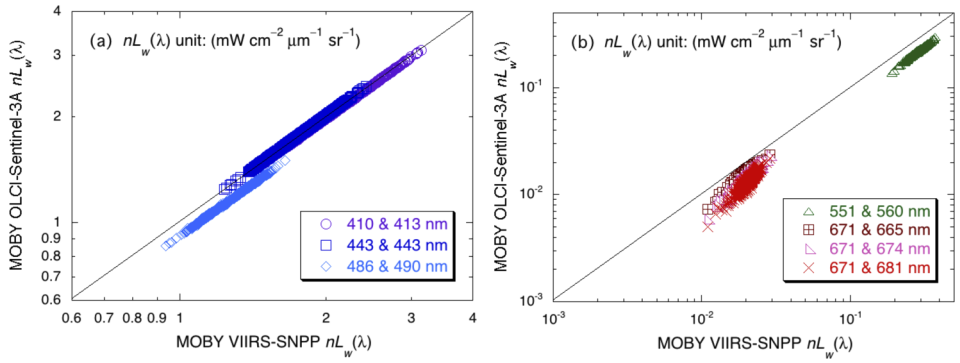

Fig. 2. Scatter plots of the MOBY-measured and sensor SRF-weighted $nL_w(\lambda)$ between OLCI-S3A and VIIRS-SNPP for the VIIRS-SNPP and OLCI-S3A spectral bands of (a) 410 & 413 nm, 443 & 443 nm, and 486 & 490 nm and (b) 551 & 560 nm, 671 & 665 nm, 671 & 674 nm, and 671 & 681 nm.

OLCI-S3A and VIIRS-SNPP. Results in Table 3 show that OLCI SRF-weighted MOBY in situ $nL_w(\lambda)$ and $\rho_{wN}(\lambda)$ at the short blue and blue bands (413 and 443 nm) are almost the same as those from VIIRS-SNPP at the bands 410 and 443 nm. They are differed ~1% over the open ocean (oligotrophic waters). These differences are quite similar to the case of VIIRS-N20 versus VIIRS-SNPP. The difference in the OLCI band at 490 nm is slightly larger (~7–9%), compared with those of VIIRS-N20 (~5%) in Table 1. However, for OLCI-S3A green and red bands, differences in $nL_w(\lambda)$ and $\rho_{wN}(\lambda)$ between OLCI- and VIIRS-SRF-weighted MOBY in situ data are quite significant, i.e., about 23%, 23%, 29%, and 35% for the OLCI bands at 560, 665, 671, and 681 nm (Table 3), respectively. They are all biased low compared with those from VIIRS-SNPP.

Table 3. Statistics in ratios (mean, median, and STD) of MOBY-measured $nL_w(\lambda)$ and $\rho_{wN}(\lambda)$ between OLCI-S3A and VIIRS-SNPP. The data number used is 512.

Spectral Band (OLCI, VIIRS) (nm)	MOBY $nL_w(\lambda)$ Ratio (OLCI versus VIIRS)			MOBY $\rho_{wN}(\lambda)$ Ratio (OLCI versus VIIRS)		
	Mean	Median	STD	Mean	Median	STD
(413, 410)	0.9883	0.9882	0.0016	0.9883	0.9883	0.0016
(443, 443)	1.0080	1.0080	0.0013	1.0111	1.0111	0.0013
(490, 486)	0.9111	0.9109	0.0044	0.9338	0.9336	0.0045
(560, 551)	0.7649	0.7654	0.0083	0.7848	0.7853	0.0085
(665, 671)	0.7759	0.7746	0.0364	0.7631	0.7619	0.0358
(674, 671)	0.7102	0.7107	0.0378	0.7150	0.7155	0.0381
(681, 671)	0.6387	0.6429	0.0490	0.6544	0.6586	0.0502

Again, similar to the case for VIIRS-N20, using the median ratio values in Table 3, all required coefficients for calculating consistent Chl-a and $K_d(490)$ data from OLCI-S3A with those from VIIRS-SNPP can be computed. These coefficients (with the corresponding applicable equations) are summarized in Table 4. Thus, using the coefficients in Table 4 for modifying the Chl-a and $K_d(490)$ algorithms, OLCI-S3A-derived Chl-a and $K_d(490)$ data are consistent with those from VIIRS-SNPP for the global open ocean.

Optics EXPRESS

Table 4. Coefficients needed for modifying various equations for the OLCI-S3A Chl-a and K_d(490) algorithms, which are calculated from Table 3 with median values.

Equation Number	Corresponding Coefficients
Eqs. (3) and (4)	$r_{24} = 0.7767$, $r_{34} = 0.8412$
Eqs. (8) and (9)	$r_2 = 0.9890$, $r_4 = 1.2734$, $r_5 = 1.3125$
Eq. (11)	$r_{24} = 0.7767$
Eq. (14)	$c_{34} = 0.8403$
Eqs. (18) and (20)	$b_3 = 0.9336$
Eqs. (19) and (20)	$b_5 = 0.7619$
Eqs. (22) and (23)	$r_{53} = 1.2254$

2.3.3. Required coefficients for SGLI-GCOM-C

The same approach can be carried out for SGLI-GCOM-C, taking VIIRS-SNPP as a reference sensor for algorithms modifications. Specifically, SGLI-GCOM-C SRF-weighted MOBY $nL_w(\lambda)$ [or $\rho_{wN}(\lambda)$] at the bands of 412, 443, 490, 566, and 672 nm are compared with the corresponding VIIRS-SNPP (SRF-weighted) bands (M1–M5) at the wavelengths of 410, 443, 486, and 551, and 671 nm, respectively. It is noted that SGLI-GCOM-C has two red bands at 672 nm, one with a low maximum radiance value (i.e., high measurement sensitivity that is applicable to ocean applications) and another with a high maximum radiance value (i.e., low measurement sensitivity that is applicable to land and atmospheric applications), corresponding to the VIIRS-SNPP red band at 671 nm. Table 5 provides these $nL_w(\lambda)$ [or $\rho_{wN}(\lambda)$] ratio values at the six SGLI bands versus the corresponding VIIRS-SNPP bands. Again, all required coefficients for calculating consistent Chl-a and K_d(490) data from SGLI-GCOM-C with those from VIIRS-SNPP can be

Table 5. Statistics in ratios (mean, median, and STD) of MOBY-measured $nL_w(\lambda)$ and $\rho_{wN}(\lambda)$ between SGLI-GCOM-C and VIIRS-SNPP. The data number used is 193.

Spectral Band (SGLI, VIIRS) (nm)	MOBY $nL_w(\lambda)$ Ratio (SGLI versus VIIRS)			MOBY $\rho_{wN}(\lambda)$ Ratio (SGLI versus VIIRS)		
	Mean	Median	STD	Mean	Median	STD
(412, 410)	0.9868	0.9868	0.0015	0.9853	0.9853	0.0015
(443, 443)	1.0070	1.0072	0.0013	1.0095	1.0097	0.0013
(490, 486)	0.9282	0.9276	0.0034	0.9527	0.9521	0.0035
(566, 551)	0.6961	0.6956	0.0087	0.7136	0.7132	0.0089
(672, 671)	0.7575	0.7570	0.0290	0.7585	0.7580	0.0290
(672, 671)	0.7571	0.7570	0.0289	0.7582	0.7581	0.0290

Table 6. Coefficients needed for modifying various equations for the SGLI-GCOM-C Chl-a and K_d(490) algorithms, which are calculated from Table 5 with median values.

Equation Number	Corresponding Coefficients
Eqs. (3) and (4)	$r_{24} = 0.7063$, $r_{34} = 0.7491$
Eqs. (8) and (9)	$r_2 = 0.9904$, $r_4 = 1.4021$, $r_5 = 1.3193$
Eq. (11)	$r_{24} = 0.7063$
Eq. (14)	$c_{34} = 0.7499$
Eqs. (18) and (20)	$b_3 = 0.9521$
Eqs. (19) and (20)	$b_5 = 0.7580$
Eqs. (22) and (23)	$r_{53} = 1.2561$

Optics EXPRESS

computed. These coefficients with the corresponding applicable equations are provided in Table 6.

3. Results

3.1. Results from MOBY in situ optics data

Using the derived coefficients in Tables 2, 4, and 6 for the corresponding applicable equations, new Chl-a and $K_d(490)$ data can be derived and evaluated using the modified algorithms for VIIRS, OLCI, and SGLI. Note that all results presented in this section are from MOBY in situ data, with specific sensor SRF data used for producing the corresponding sensor-measured data. Specifically, in situ MOBY hyperspectral optics data set was used to construct a synthetic data set of $nL_w(\lambda)$ spectra, weighted with SRFs corresponding to VIIRS-SNPP, VIIRS-N20, OLCI-S3A, and SGLI-GCOM-C. With this data set, Chl-a and $K_d(490)$ data that would be derived from VIIRS-N20, OLCI-S3A, and SGLI-GCOM-C over the MOBY site (open oceans) were compared with those from VIIRS-SNPP, i.e., we assume VIIRS-SNPP as a reference sensor. These results are presented in the following three sub-sections.

3.1.1. VIIRS-N20-derived Chl-a and $K_d(490)$

Figure 3 shows comparisons (scatter plots) for Chl-a and $K_d(490)$ calculated using the SRF-weighted VIIRS-N20 and VIIRS-SNPP MOBY in situ data. In fact, Chl-a and $K_d(490)$ data in Fig. 3 were derived using the corresponding Chl-a and $K_d(490)$ algorithms with the inputs from the MOBY in situ $nL_w(\lambda)$ spectra, which are computed with the SRF-weighted for VIIRS-N20 or VIIRS-SNPP. Specifically, Figs. 3(a) and 3(b) are Chl-a results derived from VIIRS-N20 compared with those from VIIRS-SNPP using the OC3V [19] and OCI [21] Chl-a algorithm, respectively, while Figs. 3(c) and 3(d) are $K_d(490)$ data using the open ocean $K_d(490)$ algorithm [40] and turbid coastal/inland water $K_d(490)$ algorithm [22], respectively. They show significant improvements in data consistency between VIIRS-N20 and VIIRS-SNPP Chl-a and $K_d(490)$ products. Using the original Chl-a and $K_d(490)$ algorithms, i.e., without algorithms modifications, VIIRS-N20-derived Chl-a and $K_d(490)$ data are significantly different from VIIRS-SNPP, although the spectral band differences between the two sensors are generally small. For the OC3V Chl-a algorithm, without algorithm modifications the mean difference between the two VIIRS sensors is ~30% [Fig. 3(a)], while the mean difference is ~8% for the OCI Chl-a algorithm [Fig. 3(b)] due to the fact that the CI-based Chl-a algorithm is much more tolerant to the reflectance differences between the two sensors [20,21]. For $K_d(490)$ evaluation results, without algorithm modifications differences for both the open ocean and turbid coastal/inland waters are ~15% [Figs. 3(c) and 3(d)] between the two VIIRS sensors. With the proposed approach for modifying the Chl-a and $K_d(490)$ algorithms for VIIRS-N20, both Chl-a and $K_d(490)$ data are now essentially same (consistent) from the two VIIRS sensors.

Results in Fig. 3 demonstrate that the proposed approach works perfectly in modifying the VIIRS-N20 Chl-a and $K_d(490)$ algorithms. In fact, it validates the algorithm modification approach as the MOBY in situ optics data are highly accurate, in particular, there are no errors related to the satellite ocean color data processing (e.g., atmospheric correction).

3.1.2. OLCI-S3A-derived Chl-a and $K_d(490)$

Figure 4 presents comparison results for Chl-a and $K_d(490)$ using the SRF-weighted OLCI-S3A and VIIRS-SNPP MOBY in situ data sets for cases with and without the proposed algorithm modifications. Figures 4(a) and 4(b) are the OLCI-derived Chl-a data compared with those from VIIRS-SNPP using the OC3V algorithm and OCI algorithm, respectively, while Figs. 4(c) and 4(d) are OLCI-derived $K_d(490)$ data compared with those from VIIRS-SNPP using the

Optics EXPRESS

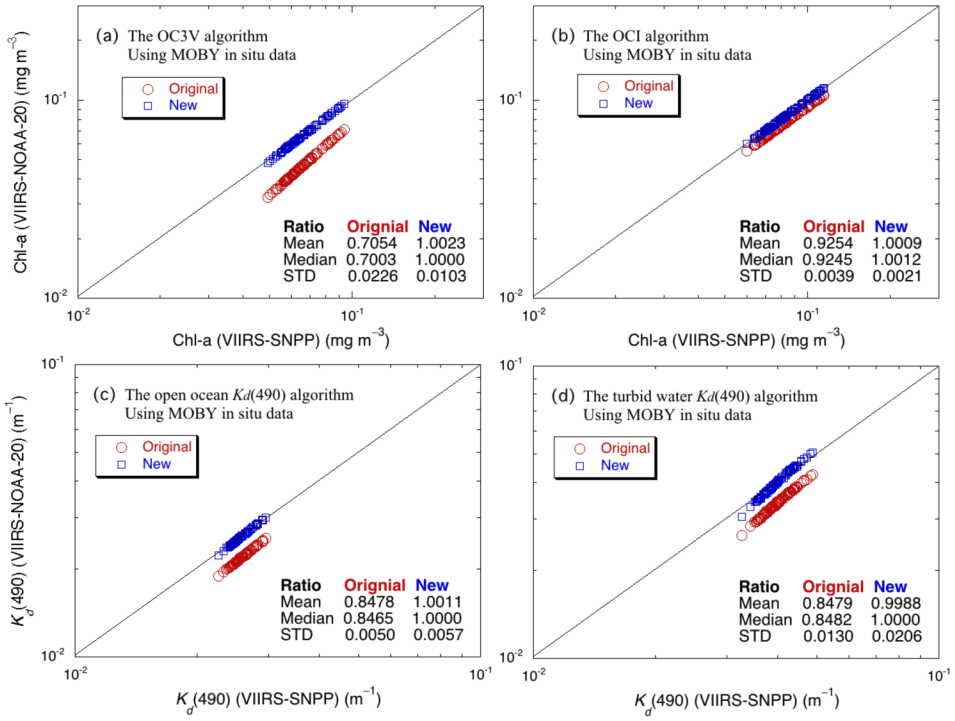

Fig. 3. Comparisons (scatter plots) of Chl-a and $K_d(490)$ between using the SRF-weighted VIIRS-N20 and VIIRS-SNPP MOBY in situ data for cases of with and without algorithms modifications for a specific product derived from (a) OC3V Chl-a algorithm, (b) OCI Chl-a algorithm, (c) open ocean $K_d(490)$ algorithm, and (d) turbid water $K_d(490)$ algorithm.

open ocean $K_d(490)$ algorithm and turbid coastal/inland water $K_d(490)$ algorithm, respectively. They are all derived using the reflectance input of the MOBY in situ optics data (the sensor SRF-weighted) for Chl-a and $K_d(490)$ algorithms. Obviously, from the results in Fig. 4, the same conclusion can be obtained as for the results in Fig. 3 for VIIRS-N20, i.e., using the proposed approach in modifying the Chl-a and $K_d(490)$ algorithms, OLCI-S3A and VIIRS-SNPP can now derive consistent Chl-a and $K_d(490)$ products. In fact, as statistics results indicated in the plots, the mean differences between OLCI-S3A and VIIRS-SNPP are improved from the original ~47%, ~17%, ~21%, and ~15% to almost all 0% for OC3V Chl-a [19], OCI Chl-a [21], open ocean $K_d(490)$ [40], and turbid coastal/inland water $K_d(490)$ algorithm [22], respectively. Indeed, these improvements are quite significant. Without algorithm modifications, OLCI- and VIIRS-derived Chl-a and $K_d(490)$ data would represent two different ocean water properties. It should also be noted that, again, Chl-a data derived using the OCI algorithm performed much better than those from the OC3V algorithm as shown in Fig. 4(b). In fact, comparing with results in Fig. 4(a) with the OC3V Chl-a algorithm, OLCI-S3A-derived Chl-a data using the OCI algorithm are more consistent with those from VIIRS-SNPP even after the algorithm modification, particularly over very low or relatively high values of Chl-a data [Fig. 4(b)].

3.1.3. SGLI-GCOM-C-derived Chl-a and $K_d(490)$

Comparison results of Chl-a and $K_d(490)$ derived using the SRF-weighted SGLI-GCOM-C and VIIRS-SNPP MOBY in situ data with and without the proposed algorithm modifications are shown in Fig. 5. Figures 5(a) and 5(b) are the SGLI-derived Chl-a data compared with those from VIIRS-SNPP using the OC3V algorithm and OCI algorithm, respectively, while Figs. 5(c)

Optics EXPRESS

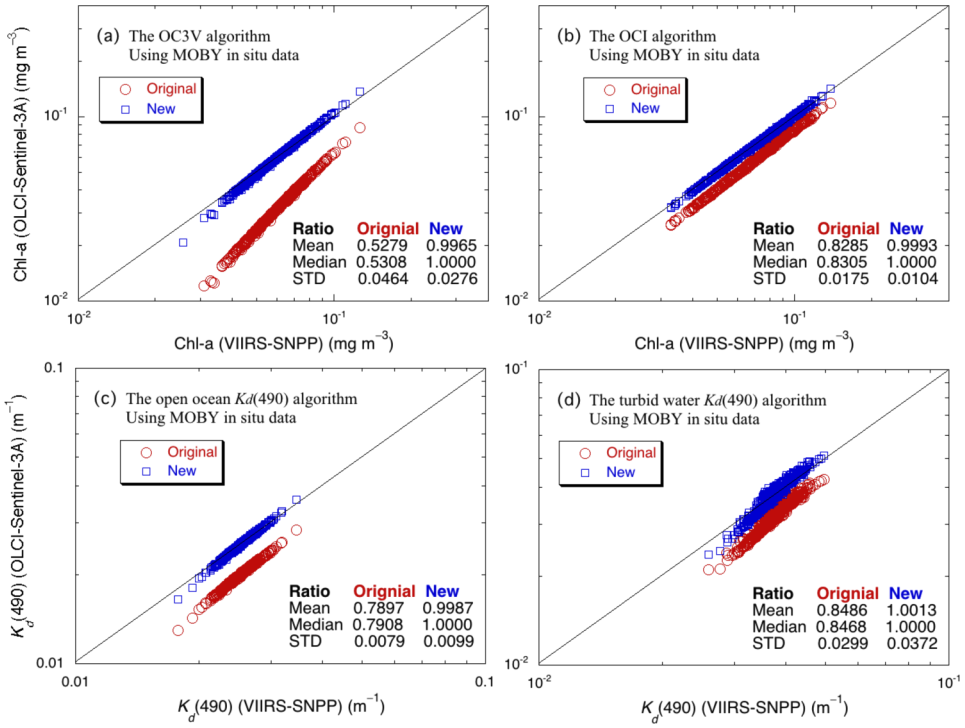

Fig. 4. Comparisons (scatter plots) of Chl-a and $K_d(490)$ between using the SRF-weighted OLCI-S3A and VIIRS-SNPP MOBY in situ optics data for cases of with and without algorithms modifications for a specific product derived from (a) OC3V Chl-a algorithm, (b) OCI Chl-a algorithm, (c) open ocean $K_d(490)$ algorithm, and (d) turbid water $K_d(490)$ algorithm.

and 5(d) are SGLI-derived $K_d(490)$ data compared with those from VIIRS-SNPP using the open ocean $K_d(490)$ algorithm and turbid water $K_d(490)$ algorithm, respectively. Again, with the proposed approach in modifying the Chl-a and $K_d(490)$ algorithms, SGLI and VIIRS produce consistent Chl-a and $K_d(490)$ products. Mean differences between SGLI and VIIRS-SNPP are improved from the original ~59%, ~21%, ~32%, and ~17% to about 0.5%, 0.1%, 0%, and 0.2% for OC3V Chl-a [19], OCI Chl-a [21], open ocean $K_d(490)$ [40], and turbid water $K_d(490)$ algorithm [22], respectively. It is concluded again that, comparing results in Fig. 5(a) with the OC3V Chl-a algorithm, SGLI-derived Chl-a data using the OCI algorithm [Fig. 5(b)] are much more consistent with those from VIIRS-SNPP even after the algorithm modification.

Furthermore, the effects of the Chl-a algorithm modifications can be demonstrated with an example for the OC3V Chl-a algorithm shown in Fig. 6. Figure 6 shows results of Chl-a as a function of the maximum reflectance ratio values [Eqs. (3) and (4)] for the original OC3V algorithm (for VIIRS-SNPP), OC3V algorithm for VIIRS-N20 (or OLCI-S3A) without modification, and OC3V algorithm with modification for a specific sensor. Results in Fig. 6 show that for both VIIRS-N20 and OLCI-S3A the coefficients for OC3V Chl-a algorithm are effectively modified such that the OC3V algorithm will have the same curve in Chl-a as a function of the maximum reflectance ratio with the input from VIIRS-SNPP, VIIRS-N20, and OLCI-S3A. In other words, the coefficients in the OC3V Chl-a algorithm are effectively changed for VIIRS-N20 and OLCI-S3A to have the same relationship of Chl-a as a function of the maximum reflectance ratio in the all three sensors (i.e., dotted line in Fig. 6) using the sensor-measured $nL_w(\lambda)$ spectra.

Optics EXPRESS

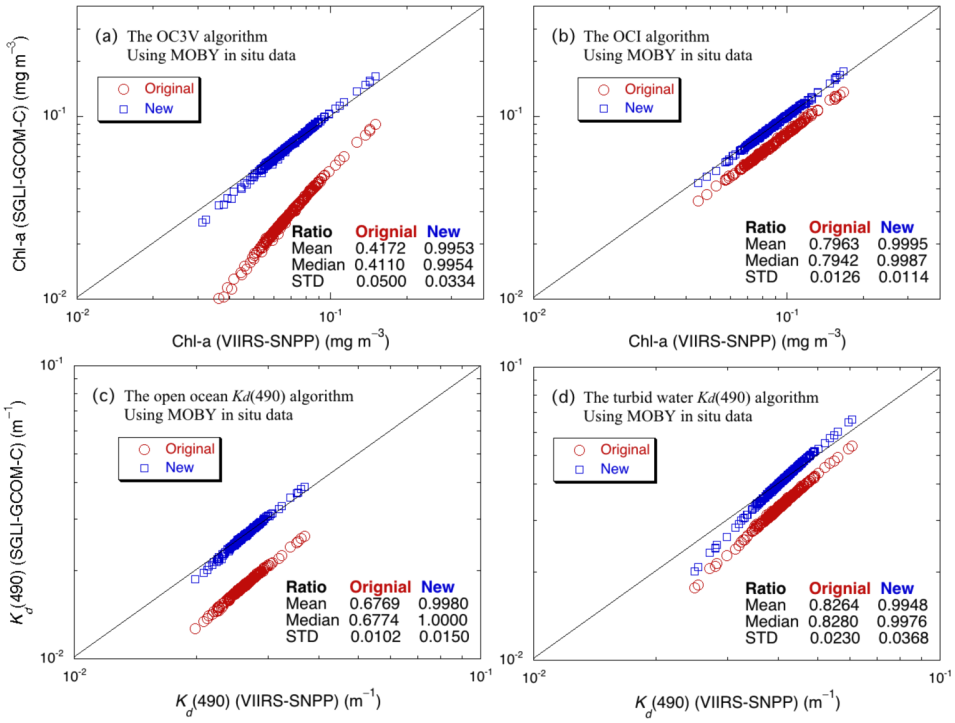

Fig. 5. Comparisons (scatter plots) of Chl-a and $K_d(490)$ between using the SRF-weighted SGLI-GCOM-C and VIIRS-SNPP MOBY in situ optics data for cases of with and without algorithms modifications for a specific product derived from (a) OC3V Chl-a algorithm, (b) OCI Chl-a algorithm, (c) open ocean $K_d(490)$ algorithm, and (d) turbid water $K_d(490)$ algorithm.

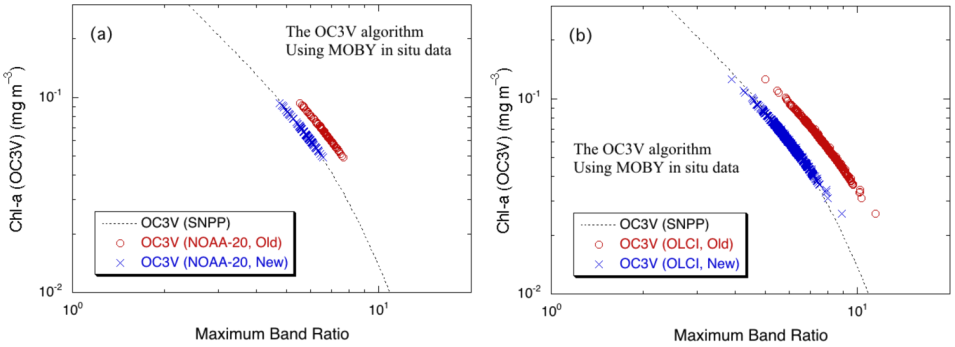

Fig. 6. Chl-a as a function of the maximum reflectance ratio value from the MOBY in situ data for VIIRS-SNPP compared with the original and modified OC3V algorithm for the satellite sensor of (a) VIIRS-N20 and (b) OLCI-S3A.

3.2. Results from satellite measurements

The proposed approach for modifying the Chl-a and $K_d(490)$ algorithms has been implemented in MSL12, in particular, for VIIRS-N20 and OLCI-S3A. The implementation of the satellite algorithms is straightforward. In fact, it can be done quite efficiently, for example, for the OC3V Chl-a algorithm, a common code for the algorithm as in Eqs. (1), (3), and (4) can be built

Optics EXPRESS

including the correction coefficients. The same code can be applied to any sensors with the corresponding coefficients, e.g., coefficients in Tables 2, 4, and 6 for VIIRS-N20, OLCI-S3A, and SGLI-GCOM-C, as well as coefficients for VIIRS-SNPP (a reference sensor) that are all set to 1. Some detailed evaluation results from VIIRS and OLCI are provided in the following two sub-sections.

3.2.1. VIIRS-N20-derived Chl-a and K_d(490) data

Figure 7 shows an example of comparison results (density plots) for VIIRS-derived ocean color products over global open oceans and coastal/inland waters on June 1, 2018 between VIIRS-N20 (with algorithm modifications) and VIIRS-SNPP. Figure 7(a) is for Chl-a data derived using the OCI Chl-a algorithm [21] and Fig. 7(b) is for K_d(490) data using the *Wang et al.* (2009) algorithm [22]. It is particularly noted that the comparisons (Fig. 7) are for all global ocean color data (open oceans and coastal/inland waters) derived on June 1, 2018. Therefore, results in Fig. 7 show that for cases of Chl-a $< \sim 0.5$ mg m^{-3} and $K_d(490) < \sim 0.3$ m^{-1}, which is usually the case for the global open ocean, with the algorithms modifications VIIRS-N20 derived Chl-a and K_d(490) data are consistent with those from VIIRS-SNPP, while for high Chl-a and K_d(490) data (usually over coastal and inland waters) there are some slightly biased high values from VIIRS-N20. In fact, quantitative comparisons show that the ratios of VIIRS-N20-derived versus VIIRS-SNPP-derived Chl-a over global deep waters (depth $\geq$ 1 km) on June 1, 2018 [Fig. 7(a)] have mean, median, and STD values of 0.9894, 0.9912, and 0.1708, respectively, while these values for K_d(490) are 1.0264, 1.0240, and 0.1076, respectively. Therefore, over global deep waters, VIIRS-N20 and VIIRS-SNPP produced consistent Chl-a and K_d(490) data on June 1, 2018. Statistical results were also computed for global coastal and inland waters (regions with water depth $<$ 1 km). For the case of June 1, 2018, the differences in VIIRS-N20- and VIIRS-SNPP-derived Chl-a and K_d(490) are about 8–10% (VIIRS-N20 biased high) as shown in Fig. 7. These comparisons were also carried out for a different day on April 30, 2018 with similar results. The statistics for both cases (April 30 and June 1, 2018) are summarized in Table 7. In Table 7, results are shown in different global ocean regions, i.e., global oligotrophic waters, global deep waters, and global coastal/inland waters, as well as data numbers used for the statistics computations. Results in Table 7 confirm the performance of the proposed approach (as results shown using the MOBY in situ data) for modifying corresponding Chl-a and K_d(490) algorithms in order to produce consistent Chl-a and K_d(490) data from the two VIIRS over global deep waters.

Table 7. Statistics results in ratios (mean, median, and STD) of VIIRS-derived Chl-a and K_d(490) between VIIRS-N20 and VIIRS-SNPP for global oligotrophic waters, deep waters, and coastal/inland waters. Data number (Num) used for statistics is also shown.

Date (in 2018)	Global Region	Num ($\times 10^5$)	VIIRS Chl-a Ratio (N20 versus SNPP)			VIIRS K_d(490) Ratio (N20 versus SNPP)		
			Mean	Median	STD	Mean	Median	STD
April 30	Oligotrophic Waters	3.12	0.9686	0.9688	0.1359	1.0129	1.0093	0.0980
	Deep Waters	8.04	0.9858	0.9883	0.1965	1.0268	1.0208	0.1170
	Coastal/Inland Waters	1.50	1.0427	1.0696	0.3300	1.0959	1.0981	0.2274
June 1	Oligotrophic Waters	3.09	0.9699	0.9728	0.1419	1.0102	1.0051	0.1017
	Deep Waters	6.82	0.9884	0.9905	0.1700	1.0257	1.0232	0.1084
	Coastal/Inland Waters	1.31	1.0497	1.0754	0.3349	1.0990	1.1069	0.2374

Furthermore, using the revised Chl-a and K_d(490) algorithms in MSL12, time series of VIIRS-N20-derived Chl-a and K_d(490) data over the global deep water (depth $\geq$ 1 km) are compared with those from VIIRS-SNPP. Figure 8 provides results of quantitative comparisons between VIIRS N20 and SNPP for Chl-a [Fig. 8(a)] and K_d(490) [Fig. 8(b)] over global deep

Optics EXPRESS

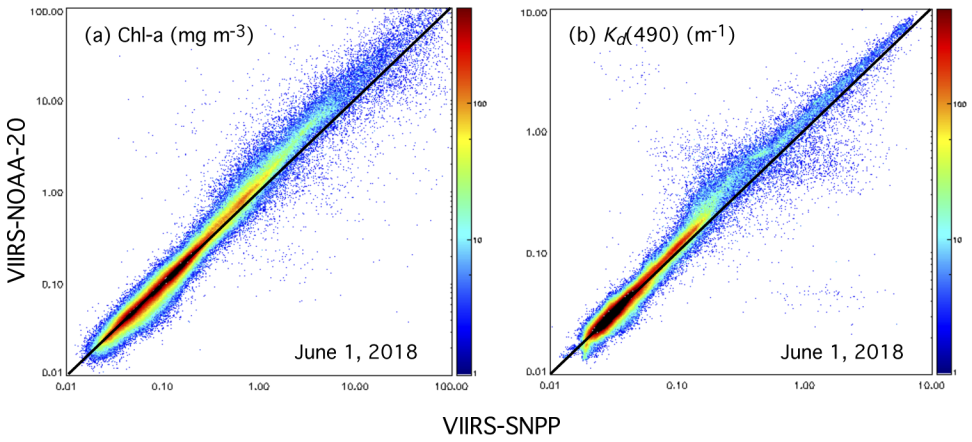

Fig. 7. Comparison results of density plot for VIIRS-derived ocean color products over global oceans and inland waters (all pixels) on June 1, 2018 between VIIRS-N20 (with algorithm modifications) and VIIRS-SNPP for data product of (a) Chl-a (OCI algorithm) and (b) $K_d(490)$.

waters for the time period of January 1 to September 30, 2018. Chl-a data were derived using the OCI Chl-a algorithm [21], and the global daily mean Chl-a and $K_d(490)$ data were derived over all daily VIIRS retrievals in the global deep water region. It is noted that, for Chl-a [Fig. 8(a)] and $K_d(490)$ [Fig. 8(b)] comparison plots, there were two significant data jumps on March 23, 2018 and April 27, 2018 for VIIRS-N20. These are due to sensor on-orbit calibration issues (not related to the ocean color data processing), i.e., significant sensor calibration jumps happened for VIIRS-N20 on these two days, leading to errors in the derived ocean color products. Results in Fig. 8 show that, from April 27, 2018 onward, VIIRS-NOAA-20-derived Chl-a and $K_d(490)$ data are consistent with those from VIIRS-SNPP over global deep waters. In fact, Chl-a and $K_d(490)$ data are essentially the same from the two VIIRS sensors, consistent with the evaluation results from the MOBY in situ data.

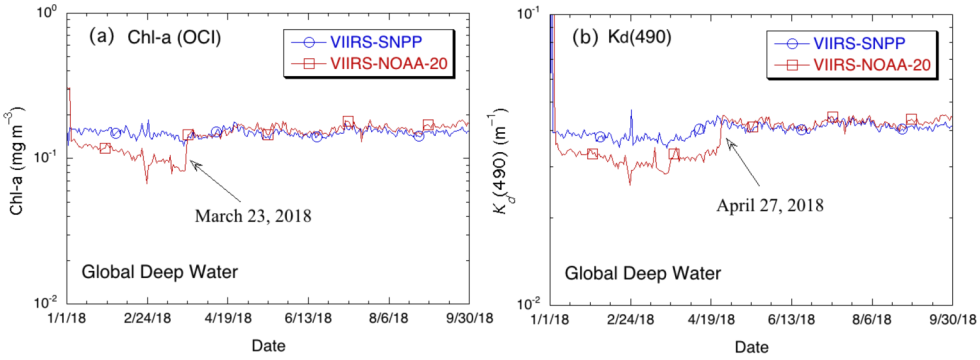

Fig. 8. Comparison results of VIIRS-derived ocean color products over global deep waters (depth ≥ 1 km) between VIIRS-N20 (with algorithm modifications) and VIIRS-SNPP for data product of (a) Chl-a and (b) $K_d(490)$.

In addition, to compare spatial distributions in the global ocean color product from the two VIIRS sensors, Figs. 9(a) and 9(b) provide the global daily Chl-a images on August 14, 2018 derived from VIIRS-SNPP and VIIRS-N20, respectively. Overall, global daily Chl-a spatial distribution from the two VIIRS sensors are quite consistent, and no obvious differences (or

Optics EXPRESS

artifacts) are observable, although data gaps from the two sensors are different. Therefore, global Chl-a and $K_d(490)$ data from VIIRS SNPP and N20 can be directly merged, as shown in Fig. 9(c) for Chl-a and Fig. 9(d) for $K_d(490)$, improving the data coverage significantly. Again, there are no observable artifacts from VIIRS SNPP and N20 merged global daily Chl-a [Fig. 9(c)] and $K_d(490)$ [Fig. 9(d)] imagers. In fact, a recent study showed that VIIRS SNPP and N20 merged global Chl-a data are quite effective and useful for capturing more details in the dynamic of ocean features [43]. Indeed, the merged VIIRS daily global Chl-a and $K_d(490)$ data, as well as global daily gap-free Chl-a data which are derived from the merged Chl-a data, are now being routinely produced [43,44].

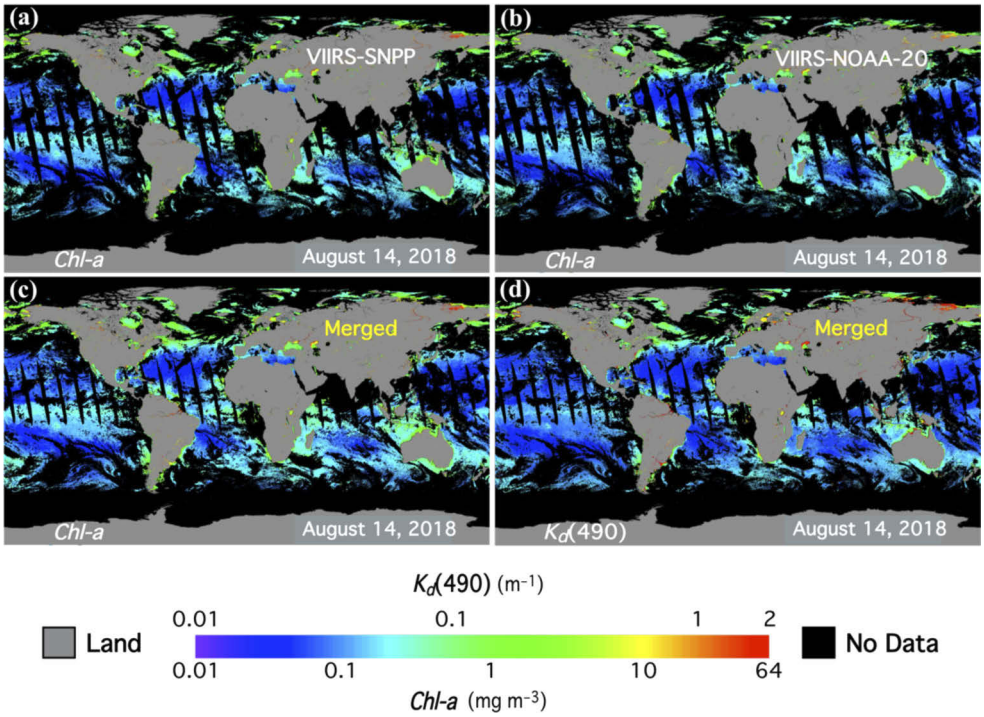

Fig. 9. Satellite-derived global daily ocean color product images on August 14, 2018 for (a) Chl-a from VIIRS-SNPP, (b) Chl-a from VIIRS-N20, (c) Chl-a from the merged VIIRS SNPP and N20, and (d) $K_d(490)$ from the merged VIIRS SNPP and N20.

3.2.2. OLCI-S3A-derived Chl-a and $K_d(490)$ over the global deep water

Figure 10 shows comparison results of OLCI-S3A- and VIIRS-SNPP-derived Chl-a [Fig. 10(a)] and $K_d(490)$ [Fig. 10(b)] data over the global deep water (depth ≥ 1 km) using the MSL12 ocean color data processing system (with and without the algorithms modifications for OLCI-S3A). VIIRS-SNPP serves as a reference sensor. Comparison results in Fig. 10 cover a time period of January–December 2018, and daily mean values of Chl-a and $K_d(490)$ were derived over all daily OLCI-S3A and VIIRS-SNPP retrievals in the global deep water region. Results in Fig. 10 clearly show the improvements with the proposed algorithm modifications for OLCI-S3A-derived Chl-a and $K_d(490)$ data over global deep waters, and further confirmed the algorithms performance as also shown in Fig. 4 using the MOBY in situ optics data (as expected), i.e., without algorithm modifications the OLCI-S3A-deirved Chl-a and $K_d(490)$ data are biased low compared with those from VIIRS-SNPP. In fact, results in Fig. 10 provide the similar conclusion that it is important to account for the sensor SRF effect on the satellite-derived ocean biological and biogeochemical

Optics EXPRESS

products in order to produce consistent ocean color products among various satellite ocean color sensors. Therefore, using the proposed algorithms, satellite-derived Chl-a and $K_d(490)$ data can be directly merged from VIIRS-SNPP, VIIRS-N20, and OLCI-S3A, further improving the global daily data coverage.

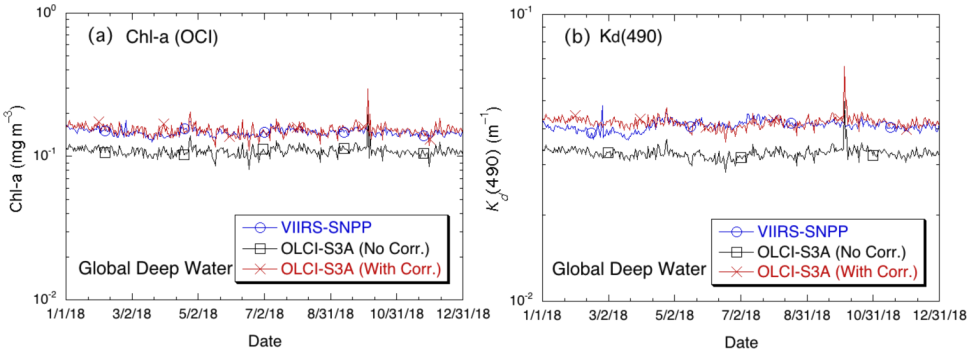

Fig. 10. Comparisons of OLCI-S3A- and VIIRS-SNPP-derived ocean color products (with and without algorithm modifications for OLCI-S3A) over global deep waters (depth ≥ 1 km) for (a) Chl-a and (b) $K_d(490)$. Note that ocean color data for both VIIRS-SNPP and OLCI-S3A are derived using the MSL12 ocean color data processing system.

4. Discussions

For different satellite ocean color sensors, there are always spectral band differences even for sensors designed to have the same spectral characteristics. Therefore, satellite-derived $nL_w(\lambda)$ [or $\rho_{wN}(\lambda)$] spectra are generally not the same among sensors, leading to some differences in retrieval of ocean biological and biogeochemical products if the corresponding algorithms are not properly adjusted. It is demonstrated in this study that, using the proposed approach for modifying Chl-a and $K_d(490)$ algorithms, satellite-derived Chl-a and $K_d(490)$ data are all consistent over global deep waters from VIIRS-SNPP, VIIRS-N20, OLCI-S3A, and SGLI-GCOM-C, although $nL_w(\lambda)$ spectra from the four sensors are different. It is noted that the algorithms performance (e.g., over various ocean regions) is not evaluated (not the purpose of this study), and readers can find many such evaluation studies, e.g., results from a round-robin algorithm comparison [45]. The major advantage for the proposed approach for modifying satellite biological and biogeochemical algorithms, as well as any other algorithms that use the input of satellite-measured $nL_w(\lambda)$ spectra, is that no corresponding in situ ocean property data are required. It is only required to have accurate hyperspectral $nL_w(\lambda)$ spectra for deriving necessary coefficients converting radiance values from one sensor to another. In addition, the derivation of the algorithm modification is rigorous assuming that the required coefficients can be derived accurately.

In fact, the basic physics for the approach is really to get satellite-derived $nL_w(\lambda)$ spectra consistent among satellite sensors for those involved for the satellite algorithms for deriving ocean/water biological and biogeochemical properties, e.g., results shown in Figs. 1 and 2. The radiance relationships among spectral bands with slight wavelength differences from various satellite sensors over the MOBY site (e.g., results presented in Figs. 1 and 2) should generally hold for open ocean (Case-1) waters, i.e., water properties described by the ocean Case-1 models [39,46]. Although the median radiance ratio values between two sensors are used for computing the required coefficients (Tables 2, 4, and 6), for some spectral bands (particularly with large spectral band differences between two sensors), linear (or even quadratic) fit may be better and required (i.e., assume non-zero intercept).

Optics EXPRESS

As discussed throughout this study, the purpose of this paper is to develop an approach for producing consistent ocean biological and biogeochemical products (or any other $nL_w(\lambda)$-based products). We used VIIRS-SNPP as a reference sensor, and Chl-a and $K_d(490)$ data derived from other satellite sensors (e.g., VIIRS-N20, OLCI-S3A, SGLI-GCOM-C, etc.) are converted to (be consistent with) those from VIIRS-SNPP. As the first sensor in the VIIRS series (and because there has been more time/effort working on the sensor), ocean color products derived from VIIRS-SNPP have been well studied, evaluated, and validated, through presentations on various conferences, meetings, and publications [47–50]. Obviously, we have much more confidence in the data quality with VIIRS-SNPP-derived ocean color products than that from VIIRS-N20. Certainly, the reference sensor may be different depending on the purpose and applications, e.g., regional studies with high spatial resolution measurements. However, no matter which sensor is used as a reference, ocean biological and biogeochemical products derived from multiple satellite sensors should all be consistent and validated to the true values, e.g., from in situ measurements. With the retrieval of consistent Chl-a and $K_d(490)$ data from various satellite ocean color sensors, product validation from one sensor (e.g., VIIRS-SNPP) can also be applied to other sensors (e.g., VIIRS-N20, OLCI-S3A, SGLI-GCOM-C, etc.). Therefore, effectively, the amount of in situ validation data can be significantly increased and the collective ocean color validation efforts from various international agencies and research groups can be used.

In this study, the coefficients for modifying the satellite biological and biogeochemical algorithms are derived using the MOBY hyperspectral in situ optics data. However, the required coefficients may also be derived using the well-established and reliable ocean modeling data, in particular, for the global open ocean for which its ocean optical and bio-optical properties are mostly driven by ocean phytoplankton properties [39,46]. However, it is always desirable and preferable to use the same ocean optics data that are used for the sensor on-orbit vicarious calibration [51–55] such as the MOBY in situ optics data [33].

In addition, since MOBY has a two-decade-long hyperspectral in situ ocean optics data set, this high quality in situ optics data may be useful for any past, present, and new satellite sensors, as long as the corresponding sensor SRFs are available. Indeed, the proposed approach for the required satellite algorithms modifications only need the sensor SRF data. This is another important advantage for the proposed approach, in particular, for the new satellite ocean color sensors, i.e., the modified satellite algorithms can be ready at the satellite launch date (only requiring sensor SRFs) and no new in situ data are really needed for this purpose.

The focus of this study is for the global open ocean because the required coefficients for the algorithm modifications are derived over the open ocean MOBY site. Over turbid coastal and inland waters, the $nL_w(\lambda)$ spectral relationships (with slightly different wavelengths) between two sensors may be different from those of the open ocean. Furthermore, water biological and biogeochemical algorithms for coastal and inland waters are usually different and much more complicated. Thus, satellite biological and biogeochemical algorithms are usually different from those discussed in this study. However, the proposed methodology can still be applied to coastal and inland waters, in particular, for the regional applications, e.g., with well-established regional $nL_w(\lambda)$ spectral relationships among satellite sensors.

It should be noted that as results have shown in Fig. 8, in particular, for the sudden jumps in Chl-a and $K_d(490)$ data on March 23, 2018 and April 27, 2018, respectively, sensor on-orbit calibration is extremely important as ocean color products are highly sensitive to the accuracy of sensor-measured radiances, i.e., sensor data records (SDR, or Level-1B data) [34]. VIIRS-SNPP SDR data were derived using the specifically improved ocean color SDR, including both solar and lunar calibrations [56]. In addition, on-orbit vicarious calibration using the MOBY in situ optics data has been carried out for VIIRS [55]. Therefore, it is important to note that the proposed approach for modifying the ocean biological and biogeochemical algorithms, as well as any other algorithms, is based on the fact that satellite-derived $nL_w(\lambda)$ spectra are accurate, in particular,

Optics EXPRESS

$nL_w(\lambda)$ spectra from multiple satellite ocean color sensors are derived consistently (e.g., using the same MSL12 for ocean color data processing).

5. Conclusion

A methodology is developed to account for the differences in the specifics of sensor spectral characteristics from multiple satellite ocean color sensors. It is assumed that satellite sensors have common spectral bands for remote sensing of global ocean optical, biological, and biogeochemical properties. Therefore, differences in these common spectral bands for ocean color remote sensing are generally not significant. The differences in sensor spectral characteristics from different satellite sensors always exist even for the same satellite series that is designed to have the same sensor spectral characteristics, e.g., VIIRS on the SNPP and JPSS series, OLCI on the Sentinel-3 series, etc. To account for the effects of sensor spectral band differences on the satellite biological and biogeochemical algorithms, e.g., Chl-a and $K_d(490)$ algorithms, the formulas for the algorithm modifications are rigorously derived, and the required coefficients are obtained from high accurate MOBY hyperspectral in situ optics data set (for global open ocean waters).

Evaluation results show that, using the proposed approach for modifying the Chl-a and $K_d(490)$ algorithms, VIIRS-N20- and OLCI-S3A-derived Chl-a and $K_d(490)$ data are consistent with those from VIIRS-SNPP for the MOBY site and over global deep waters. Therefore, global Chl-a and $K_d(490)$ data can be directly merged from the two VIIRS sensors, and there are no observable artifacts from the merged ocean color products. In addition, OLCI-S3A-derived global Chl-a and $K_d(490)$ may also be merged with those from the two VIIRS, further improving the data coverage. With the proposed algorithm modifications, SGLI-GCOM-C-derived Chl-a and $K_d(490)$ are evaluated and are consistent with those from VIIRS-SNPP over the MOBY site.

Finally, it is important to note that using the mission-long MOBY in situ optics data (1997–present) the proposed approach for the algorithm modifications can be used for any past, present, and new satellite ocean color sensors, as long as the specific sensor SRFs are available. Therefore, using the proposed approach, the modified algorithms can be ready before the launch of new satellite sensors.

Funding

Joint Polar Satellite System (JPSS).

Acknowledgments

The authors are grateful to the MOBY team for providing the in situ data in support of various satellite ocean color missions. We thank three anonymous reviewers for their useful comments. The views, opinions, and findings contained in this paper are those of the authors and should not be construed as an official NOAA or U.S. Government position, policy, or decision.

References

1. H. R. Gordon and M. Wang, "Retrieval of water-leaving radiance and aerosol optical thickness over the oceans with SeaWiFS: A preliminary algorithm," Appl. Opt. **33**(3), 443–452 (1994).
2. M. Wang, "Remote sensing of the ocean contributions from ultraviolet to near-infrared using the shortwave infrared bands: simulations," Appl. Opt. **46**(9), 1535–1547 (2007).
3. IOCCG, *Atmospheric Correction for Remotely-Sensed Ocean-Colour Products*, M. Wang (Ed.), Reports of International Ocean-Color Coordinating Group, No. 10, IOCCG, Dartmouth, Canada, doi:10.25607/OBP-101 (2010).
4. D. Antoine and A. Morel, "A multiple scattering algorithm for atmospheric correction of remotely sensed ocean colour (MERIS instrument): principle and implementation for atmospheres carrying various aerosols including absorbing ones," Int. J. Remote Sens. **20**(9), 1875–1916 (1999).
5. H. Fukushima, A. Higurashi, Y. Mitomi, T. Nakajima, T. Noguchi, T. Tanaka, and M. Toratani, "Correction of atmospheric effects on ADEOS/OCTS ocean color data: Algorithm description and evaluation of its performance," J. Oceanogr. **54**(5), 417–430 (1998).

Optics EXPRESS

6. G. Thuillier, M. Herse, D. Labs, T. Foujols, W. Peetermans, D. Gillotay, P. C. Simon, and H. Mandel, "The solar spectral irradiance from 200 to 2400 nm as measured by the SOLSPEC spectrometer from the ATLAS and EURECA missions," Sol. Phys. **214**(1), 1–22 (2003).
7. A. Morel and G. Gentili, "Diffuse reflectance of oceanic waters. III. Implication of bidirectionality for the remote-sensing problem," Appl. Opt. **35**(24), 4850–4862 (1996).
8. H. R. Gordon, "Normalized water-leaving radiance: revisiting the influence of surface roughness," Appl. Opt. **44**(2), 241–248 (2005).
9. M. Wang, "Effects of ocean surface reflectance variation with solar elevation on normalized water-leaving radiance," Appl. Opt. **45**(17), 4122–4128 (2006).
10. M. D. Goldberg, H. Kilcoyne, H. Cikanek, and A. Mehta, "Joint Polar Satellite System: The United States next generation civilian polar-orbiting environmental satellite system," J. Geophys. Res.: Atmos. **118**(24), 13,463–13,475 (2013).
11. C. R. McClain, G. C. Feldman, and S. B. Hooker, "An overview of the SeaWiFS project and strategies for producing a climate research quality global ocean bio-optical time series," Deep Sea Res., Part II **51**(1-3), 5–42 (2004).
12. V. V. Salomonson, W. L. Barnes, P. W. Maymon, H. E. Montgomery, and H. Ostrow, "MODIS: advanced facility instrument for studies of the Earth as a system," IEEE Trans. Geosci. Electron. **27**(2), 145–153 (1989).
13. W. E. Esaias, M. R. Abbott, I. Barton, O. B. Brown, J. W. Campbell, K. L. Carder, D. K. Clark, R. L. Evans, F. E. Hodge, H. R. Gordon, W. P. Balch, R. Letelier, and P. J. Minnet, "An overview of MODIS capabilities for ocean science observations," IEEE Trans. Geosci. Electron. **36**(4), 1250–1265 (1998).
14. M. Rast, J. L. Bezy, and S. Bruzzi, "The ESA Medium Resolution Imaging Spectrometer MERIS a review of the instrument and its mission," Int. J. Remote Sens. **20**(9), 1681–1702 (1999).
15. C. Donlon, B. Berruti, A. Buongiorno, M.-H. Ferreira, P. Femenias, J. Frerick, P. Goryl, U. Klein, H. Laur, C. Mavrocordatos, J. Nieke, H. Rebhan, B. Seitz, J. Stroede, and R. Sciarra, "The Global Monitoring for Environment and Security (GMES) Sentinel-3 mission," Remote Sens. Environ. **120**, 37–57 (2012).
16. J. K. Choi, Y. J. Park, J. H. Ahn, H. S. Lim, J. Eom, and J. H. Ryu, "GOCI, the world's first geostationary ocean color observation satellite, for the monitoring of temporal variability in coastal water turbidity," J. Geophys. Res. **117**(C9), 1 (2012).
17. M. Wang, J. H. Ahn, L. Jiang, W. Shi, S. Son, Y. J. Park, and J. H. Ryu, "Ocean color products from the Korean Geostationary Ocean Color Imager (GOCI)," Opt. Express **21**(3), 3835–3849 (2013).
18. M. Wang, B. A. Franz, R. A. Barnes, and C. R. McClain, "Effects of spectral bandpass on SeaWiFS-retrieved near-surface optical properties of the ocean," Appl. Opt. **40**(3), 343–348 (2001).
19. J. E. O'Reilly, S. Maritorena, B. G. Mitchell, D. A. Siegel, K. L. Carder, S. A. Garver, M. Kahru, and C. R. McClain, "Ocean color chlorophyll algorithms for SeaWiFS," J. Geophys. Res. **103**(C11), 24937–24953 (1998).
20. C. Hu, Z. Lee, and B. A. Franz, "Chlorophyll a algorithms for oligotrophic oceans: A novel approach based on three-band reflectance difference," J. Geophys. Res. **117**(C1), C01011 (2012).
21. M. Wang and S. Son, "VIIRS-derived chlorophyll-a using the ocean color index method," Remote Sens. Environ. **182**, 141–149 (2016).
22. M. Wang, S. Son, and J. L. W. Harding, "Retrieval of diffuse attenuation coefficient in the Chesapeake Bay and turbid ocean regions for satellite ocean color applications," J. Geophys. Res. **114**(C10), C10011 (2009).
23. Z. P. Lee, M. Darecki, K. Carder, C. Davis, D. Stramski, and W. Rhea, "Diffuse attenuation coefficient of downwelling irradiance: An evaluation of remote sensing methods," J. Geophys. Res. **110**(C2), C02017 (2005).
24. A. Morel, Y. Huot, B. Gentili, P. J. Werdell, S. B. Hooker, and B. A. Franz, "Examining the consistency of products derived from various ocean color sensors in open ocean (Case 1) waters in the perspective of a multi-sensor approach," Remote Sens. Environ. **111**(1), 69–88 (2007).
25. S. Son and M. Wang, "Diffuse attenuation coefficient of the photosynthetically available radiation Kd(PAR) for global open ocean and coastal waters," Remote Sens. Environ. **159**, 250–258 (2015).
26. J. E. O'Reilly, S. Maritorena, D. A. Siegel, M. C. O'Brien, D. Toole, B. G. Mitchell, M. Kahru, F. P. Chavez, P. Strutton, G. F. Cota, S. B. Hooker, C. R. McClain, K. L. Carder, F. Muller-Karger, L. Harding, A. Magnuson, D. Phinney, G. F. Moore, J. Aiken, K. R. Arrigo, R. Letelier, and M. Culver, "Ocean Colr Chlorophyll a Algorithms for SeaWiFS, OC2 and OC4: Version 4," (S. B. Hooker and E. R. Firestone, eds., NASA Goddard Space Flight Center, Greenbelt, Maryland, 2000), pp. 8–22.
27. J. E. O'Reilly and P. J. Werdell, "Chlorophyll algorithms for ocean color sensors - OC4, OC5 & OC6," Remote Sens. Environ. **229**, 32–47 (2019).
28. Z. P. Lee, K. L. Carder, and R. A. Arnone, "Deriving inherent optical properties from water color: a multiple quasi-analytical algorithm for optically deep waters," Appl. Opt. **41**(27), 5755–5772 (2002).
29. S. Maritorena, D. A. Siegel, and A. Peterson, "Optimization of a semi-analytical ocean color model for global scale applications," Appl. Opt. **41**(15), 2705–2714 (2002).
30. W. Shi and M. Wang, "A blended inherent optical property algorithm for global satellite ocean color observations," Limnol. Oceanogr.: Methods **17**, 377–394 (2019).
31. P. J. Werdell, B. A. Franz, S. W. Bailey, G. C. Feldman, E. Boss, V. E. Brando, M. Dowell, T. Hirata, S. J. Lavender, Z. P. Lee, H. Loisel, S. Maritorena, F. Melin, T. S. Moore, T. J. Smyth, D. Antoine, E. Devred, O. H. F. d'Andon, and A. Mangin, "Generalized ocean color inversion model for retrieving marine inherent optical properties," Appl. Opt. **52**(10), 2019–2037 (2013).

Optics EXPRESS

32. X. Yu, Z. Lee, F. Shen, M. Wang, J. Wei, L. Jiang, and Z. Shang, "An empirical algorithm to seamlessly retrieve the concentration of suspended particulate matter from water color across ocean to turbid river mouths," Remote Sens. Environ. **235**, 111491 (2019).
33. D. K. Clark, H. R. Gordon, K. J. Voss, Y. Ge, W. Broenkow, and C. Trees, "Validation of atmospheric correction over the ocean," J. Geophys. Res. **102**(D14), 17209–17217 (1997).
34. M. Wang, X. Liu, L. Tan, L. Jiang, S. Son, W. Shi, K. Rausch, and K. Voss, "Impact of VIIRS SDR performance on ocean color products," J. Geophys. Res.: Atmos. **118**(18), 10,347–10,360 (2013).
35. M. Wang, "A sensitivity study of SeaWiFS atmospheric correction algorithm: Effects of spectral band variations," Remote Sens. Environ. **67**(3), 348–359 (1999).
36. M. Wang and B. A. Franz, "Comparing the ocean color measurements between MOS and SeaWiFS: A vicarious intercalibration approach for MOS," IEEE Trans. Geosci. Electron. **38**(1), 184–197 (2000).
37. M. Wang, A. Isaacman, B. A. Franz, and C. R. McClain, "Ocean color optical property data derived from the Japanese Ocean Color and Temperature Scanner and the French Polarization and Directionality of the Earth's Reflectances: A comparison study," Appl. Opt. **41**(6), 974–990 (2002).
38. H. R. Gordon and A. Morel, *Remote assessment of ocean color for interpretation of satellite visible imagery: A review*, (Springer-Verlag, New York 1983).
39. H. R. Gordon, O. B. Brown, R. H. Evans, J. W. Brown, R. C. Smith, K. S. Baker, and D. K. Clark, "A semianalytic radiance model of ocean color," J. Geophys. Res. **93**(D9), 10909–10924 (1988).
40. J. L. Mueller, "SeaWiFS algorithm for the diffuse attenuation coefficient, K(490), using water-leaving radiances at 490 and 555 nm," (NASA Goddard Space Flight Center, Greenbelt, Maryland, 24–27 (2000).
41. C. D. Mobley, *Light and Water: Radiative Transfer in Natural Waters*, (Academic, New York 1994).
42. H. Loisel and A. Morel, "Non-isotropy of the upward radiance field in typical coastal (Case 2) waters," Int. J. Remote Sens. **22**(2-3), 275–295 (2001).
43. X. Liu and M. Wang, "Filling the gaps of missing data in the merged VIIRS SNPP/NOAA-20 ocean color product using the DINEOF method," Remote Sens. **11**(2), 178 (2019).
44. X. Liu and M. Wang, "Gap filling of missing data for the VIIRS global ocean color products using the DINEOF method," IEEE Trans. Geosci. Electron. **56**(8), 4464–4476 (2018).
45. R. J. W. Brewin, S. Sathyendranath, D. Muller, C. Brockmann, P. Y. Deschamps, E. Devred, R. Doerffer, N. Fomferra, B. A. Franz, M. Grant, S. Groom, A. Horseman, C. Hu, H. Krasemann, Z. Lee, S. Maritorena, F. Melin, M. Peters, T. Platt, P. Regner, T. Smyth, F. Steinmetz, J. Swinton, J. Werdell, and G. N. White III, "The ocean colour climate change initiative: III. A round-robin comparison on in-water bio-optical algorithms," Remote Sens. Environ. **162**, 271–294 (2015).
46. A. Morel and S. Maritorena, "Bio-optical properties of oceanic waters: A reappraisal," J. Geophys. Res. **106**(C4), 7163–7180 (2001).
47. S. Hlaing, T. Harmel, A. Gilerson, R. Foster, A. Weidemann, R. Arnone, M. Wang, and S. Ahmed, "Evaluation of the VIIRS ocean color monitoring performance in coastal regions," Remote Sens. Environ. **139**, 398–414 (2013).
48. M. Wang, L. Jiang, X. Liu, S. Son, J. Sun, W. Shi, L. Tan, K. Mikelsons, X. Wang, and V. Lance, "VIIRS ocean color products: A progress update," *Proc. the IEEE Int. Geosci. Remote Sens. Symposium (IGARSS)*, http://dx.doi.org/10.1109/IGARSS.2016.7730528, 5848–5851, Beijing, China, July 5810-5815 (2016).
49. B. B. Barnes, J. P. Cannizzaro, D. C. English, and C. Hu, "Validation of VIIRS and MODIS reflectance data in coastal and oceanic waters: An assessment of methods," Remote Sens. Environ. **220**, 110–123 (2019).
50. K. Mikelsons, M. Wang, and L. Jiang, "Statistical evaluation of satellite ocean color data retrievals," Remote Sens. Environ. **237**, 111601 (2020).
51. H. R. Gordon, "In-orbit calibration strategy for ocean color sensors," Rem. Sens. Environ. **63**(3), 265–278 (1998).
52. M. Wang and H. R. Gordon, "Calibration of ocean color scanners: How much error is acceptable in the near-infrared," Remote Sens. Environ. **82**(2-3), 497–504 (2002).
53. B. A. Franz, S. W. Bailey, P. J. Werdell, and C. R. McClain, "Sensor-independent approach to the vicarious calibration of satellite ocean color radiometry," Appl. Opt. **46**(22), 5068–5082 (2007).
54. G. Zibordi, F. Melin, K. Voss, B. C. Johnson, B. A. Franz, E. Kwiatkowska, J. P. Huot, M. Wang, and D. Antoine, "System vicarious calibration for ocean color climate change applications: Requirements for in situ data," Remote Sens. Environ. **159**, 361–369 (2015).
55. M. Wang, W. Shi, L. Jiang, and K. Voss, "NIR- and SWIR-based on-orbit vicarious calibrations for satellite ocean color sensors," Opt. Express **24**(18), 20437–20453 (2016).
56. J. Sun and M. Wang, "Radiometric calibration of the VIIRS reflective solar bands with robust characterizations and hybrid calibration coefficients," Appl. Opt. **54**(31), 9331–9342 (2015).